Tracheal motile cilia require CAMSAP3 for formation of central microtubule pair and coordinated beating

Hiroko Saito[1], Fumiko Matsukawa-Usami[2], Toshihiko Fujimori[2], Toshiya Kimura[1], Takahiro Ide[3], Takaki Yamamoto[4], Tatsuo Shibata[5], Kenta Onoue[6], Satoko Okayama[6], Shigenobu Yonemura[6], Kazuyo Misaki[7], Mika Toya[1,8], and Masatoshi Takeichi[1]

[1]Laboratory for Cell Adhesion and Tissue Patterning, RIKEN Center for Biosystems Dynamics Research, 2-2-3 Minatojima-Minamimachi, Chuo-ku, Kobe 650-0047, Japan

[2]Division of Embryology, National Institute for Basic Biology, and Department of Basic Biology, School of Life Science, SOKENDAI, the Graduate University for Advanced Studies, 5-1 Higashiyama, Myodaiji-cho, Okazaki, 444-8787 Japan

[3]Laboratory for Organismal Patterning, RIKEN Center for Biosystems Dynamics Research, 2-2-3 Minatojima-Minamimachi, Chuo-ku, Kobe 650-0047, Japan

[4]Nonequilibrium Physics of Living Matter RIKEN Hakubi Research Team, RIKEN Center for Biosystems Dynamics Research, Kobe 650-0047, Japan

[5]Laboratory for Physical Biology, RIKEN Center for Biosystems Dynamics Research, 2-2-3 Minatojima-Minamimachi, Chuo-ku, Kobe 650-0047, Japan

[6]Laboratory for Ultrastructural Research, RIKEN Center for Biosystems Dynamics Research, 2-2-3 Minatojima-Minamimachi, Chuo-ku, Kobe 650-0047, Japan

[7]Ultrastructural Research Team, RIKEN Center for Life Science Technologies, 2-2-3 Minatojima-Minamimachi, Chuo-ku, Kobe 650-0047, Japan

[8]Major in Bioscience, Global Center for Science and Engineering, Faculty of Science and Engineering, Waseda University, 3-4-1 Okubo, Shinjukuku, Tokyo 169-8555, Japan

Correspondence to:

Masatoshi Takeichi
RIKEN Center for Biosystems Dynamics Research,
2-2-3 Minatojima-Minamimachi, Chuo-ku,
Kobe 650-0047, Japan.
e-mail: masatoshi.takeichi@riken.jp
phone: 81(78) 306-3116
fax: 81(78) 306-3118

Abstract

Motile cilia of multiciliated epithelial cells undergo synchronized beating to produce fluid flow along the luminal surface of various organs. Each motile cilium consists of an axoneme and a basal body, which are linked by a 'transition zone'. The axoneme exhibits a characteristic 9+2 microtubule arrangement important for ciliary motion, but how this microtubule system is generated is not yet fully understood. Here, using superresolution microscopy, we show that CAMSAP3, a protein that can stabilize the minus end of a microtubule, concentrates at multiple sites of the cilium-basal body complex, including the upper region of the transition zone or the axonemal basal plate where the central pair of microtubules (CP) terminates. CAMSAP3 dysfunction resulted in loss of the CP and partial distortion of the basal plate, as well as the failure of multicilia to undergo synchronized beating. These findings indicate that CAMSAP3 plays pivotal roles in the formation or stabilization of the CP, and thereby supports the coordinated motion of multicilia in airway epithelial cells.

Introduction

Multiciliated cells play a central role in generating directional flow of fluids or particles over the surface of various epithelial tissues, such as oviduct epithelium, ependymal cells lining the brain ventricles, and the airway epithelium of the respiratory tract (Brooks and Wallingford, 2014). Motile cilia on these epithelial cells beat synchronously to produce hydrodynamic forces. Failure of cilia to undergo their

coordinated movement causes various diseases, which are collectively called primary ciliary dyskinesia (PCD) (Damseh et al., 2017; Lee, 2011; Tilley et al., 2015).

The individual motile cilium of multiciliated cells consists of a 9+2 microtubule arrangement, that is, nine microtubule doublets and a central pair of single microtubules, which position at the outer and central zones, respectively. This core structure of a cilium, called an axoneme, is linked to the basal body, a form of centriole, from which ciliogenesis begins during development (Dawe et al., 2007a). The connection between the axoneme and the basal body is mediated by a zone called the 'transition zone (TZ)' (Czarnecki and Shah, 2012; Goncalves and Pelletier, 2017), and the central pair of microtubules (CP) terminates just above the TZ, although the outer microtubules extend farther downward to join the triplet microtubules of the basal body (Greenan et al., 2020). Although extensive studies have been conducted to understand how these ciliary structures form and how motile cilia move in a coordinated fashion (Satir and Christensen, 2007), the molecular mechanisms underlying these questions are still largely unresolved.

CP deficiency brings about defective motion of cilia or flagella (Dawe et al., 2007b; Lechtreck et al., 2008; Loreng and Smith, 2017; Nozawa et al., 2013; Smith and Yang, 2004), and is also associated with PCD (Bautista-Harris et al., 2000; Burgoyne et al., 2014; Stannard et al., 2004). How the CP grows out from the TZ in motile cilia, however, remains unknown, particularly because no template for microtubule polymerization is detected at the TZ.

CAMSAP (calmodulin-regulated spectrin-associated protein) and its invertebrate relatives form a protein family, each member of which binds the minus end of non-centrosomal microtubules (Baines et al., 2009; Goodwin and Vale, 2010; Hendershott and Vale, 2014; Jiang et al., 2014; King et al., 2014; Meng et al., 2008; Richardson et al., 2014; Tanaka et al., 2012). Through this property of CAMSAP, it regulates the dynamics of the minus ends of microtubules, simultaneously anchoring them to particular subcellular sites (Nashchekin et al., 2016; Toya et al., 2016), and contributes to a variety of cell and tissue morphogenesis (Kimura et al., 2021; Ko et al., 2019; Martin et al., 2018; Mitsuhata et al., 2021; Noordstra et al., 2016; Takeda et al., 2018), including neuritegenesis (Chen et al., 2020; Chuang et al., 2014; Feng et al., 2019; Pongrakhananon et al., 2018; Wang et al., 2019; Yau et al., 2014). In vertebrate epithelial cells, CAMSAP3, a member of this molecular family, is concentrated at apical cortical regions, tethering non-centrosomal microtubules to these sites (Toya et al., 2016), resulting in the assembly of microtubules whose plus ends point basally. This characteristic microtubule assembly is disrupted in mice bearing a mutant gene encoding a truncated *Camsap3* (*Camsap3*$^{dc/dc}$ mice), in which the C-terminal microtubule-binding CKK domain is deleted (Toya et al., 2016).

A recent study showed that CAMSAP3 is expressed in nasal multiciliated cells and its absence causes defects in ciliary motion and polarity (Robinson et al., 2020). Similar observations were also reported using oviduct cells (Usami et al., 2021). However, how CAMSAP3 regulates the structure and function of multicilia remains to be investigated. In the present study, we used airway epithelial cells of adult mice to elucidate the role of CAMSAP3 in coordinated movement of multicilia, finding that CAMSAP3 dysfunction

results in a partial disruption of axonemal structures at its proximal end, as well as loss of the CP. Superresolution microscopy revealed that a fraction of CAMSAP3 accumulates around the site where the CP is supposed to be anchored. Based on these observations, we discuss potential mechanisms by which CAMSAP3 regulates CP formation and coordinated motion of multicilia.

Results

Defective ciliary motion in *Camsap3*-mutated airway cells

Camsap3$^{dc/dc}$ mutant mice frequently produced clicking or chattering sounds (Audio 1), suggesting that they might have respiratory problems. We examined the luminal surface of trachea collected from postnatal mice using scanning electron-microscopy, finding that multiciliated epithelial cells are normally present in the trachea of *Camsap3*$^{dc/dc}$ mice, the distribution pattern of which was similar to that observed in wild-type trachea (Fig. 1A). In higher magnification views, however, we noted that the alignment of multicilia along the longitudinal axis of trachea, which is generally well ordered in wild-type airway cells, was somewhat disorganized in *Camsap3*-mutated cells (Fig. 1A).

To examine whether the cilia of the mutant cells have any defects in motility, we isolated trachea and acquired time-lapse images of the cilia on airway epithelial cells. Wild-type cells exhibited a characteristic synchronized beating of multicilia (Movie 1), whereas those of *Camsap3*$^{dc/dc}$ cells tended to lose such orderly motion, instead

displaying aberrant movements individually (Movie 2). We then analyzed these movies to quantify the pattern of ciliary motion by calculating the flow field of a ciliary carpet using particle image velocimetry (PIV). The flow field for a wild-type cell showed that multiple cilia on the cell oscillated together collectively (Fig. 1B and Movie 3). In contrast, those in a mutant cell were subdivided into several smaller clusters, each of which showed a collective flow in a unique direction (Fig. 1B and Movie 4). Using these data, we quantified the degree of synchrony of ciliary motion by calculating the time-evolution of the average speed of the motion, which is the magnitude of the average velocity over the field of view. Since the individual cilia drive oscillatory motion in the flow field of PIV, if all ciliary motions are synchronized, the magnitude of the average velocity vector is expected to show oscillation. In contrast, if the ciliary motion is all spatially random, the magnitude of average velocity vector would not oscillate in time. Our analysis showed that the magnitude of the average velocity vector oscillated less prominently in the mutant than in the wild-type cells, indicating that the degree of synchrony of ciliary motion was lower in the mutant cells (Fig. 1C).

Loss of the central microtubule pair in the axoneme of *Camsap3*-mutated cilia

To investigate the structural basis underlying the uncoordinated beating of cilia in *Camsap3*$^{dc/dc}$ cells, we used transmission microscopy. Longitudinal sections along the cilia revealed that the overall morphology of cilia and basal bodies looked normal in the mutants. However, the centrally located electron-dense signals that represent the central pair of microtubules (CP) were not clearly detectable in the mutant cells, as they were often discontinuous (Fig. 2A). Cross sections of cilia revealed further details of such abnormalities, showing that the CP was not detectable in any cilium of mutant cells. In

these cells, 70% of cilia did not show any central structure, and the remaining fraction of cilia exhibited an 8+1 microtubule organization in which the central microtubules looked like the outer doublet microtubules in their configuration (Fig. 2B). These abnormal central microtubules were occasionally located at non-central positions.

To seek the origin of these anomalous central microtubules, we reexamined longitudinal sections and found that, when central microtubules are still detectable, they are tilted along the longitudinal axis, one end of which gets closer to peripheral regions of the axoneme around its basal positions (Fig. 2C). These observations suggest the possibility that an outer microtubule doublet was abnormally internalized to form the central one, as observed in PCD (Burgoyne et al., 2014).

We then focused on the proximal zones of axonemes, where the CP is thought to be nucleated. In longitudinal sections, the CP ended at a zone characterized by the accumulation of electron-dense materials at around the outer microtubule doublets (Fig. 2A left, dark arrow). As this zone positionally corresponds to the 'basal plate' or 'axonemal plate' that is observed in cilia of unicellular organisms and thought to be the site for CP nucleation (Dean et al., 2016; Dute and Kung, 1978; Gilula and Satir, 1972; Hoog et al., 2014; Tucker, 1971), we also call it 'basal plate (BP)', although this structure appears to have a cylindrical shape in the case of airway cells. Closer observations showed that the CP terminated at around the basal end of the BP, but was often sticking out of this BP structure by 20 nm or so (Fig. 2A, white arrow in the enlarged image). Axonemes in *Camsap3*-mutated cells appeared to have a similar zone,

except that microtubules were not always detectable in the BP of mutant samples, as seen in upper axonemal zones (Fig. 2A right, dark arrow).

To confirm these observations, we used transverse sections of an airway cell which are slightly tilted, as these allowed us to observe sequential changes in the inner structures of cilium and basal body along the longitudinal axis within a single focal plane. In wild-type samples, we detected a group of ciliary sections, each of which exhibits an electron-dense outer ring with a central core (Fig. 2D, left), just as seen in the BP defined above, leading us to judge that these are transverse views of the BP. In the cilia of *Camsap3*$^{dc/dc}$ cells, these structures were deformed showing various abnormalities, such as a missing central core, overly condensed central materials, and partial distortion of the outer ring (Fig. 2D, right). Thus, not only the CP but also the entire BP architecture appeared abnormal in the mutant. On the other hand, we did not detect any clear abnormities in the subdivisions of the cilium-basal body complex located below the BP, including the transition zone (TZ), except that the basal bodies tended to lose their planar polarity in mutant cells, as assessed by the direction of the 'basal foot' which normally faces the oral side in wild-type cells (Fig. 2E).

Concentration of CAMSAP3 around the proximal ends of cilia

To begin investigating how CAMSAP3 contributes to microtubule assembly in axonemes, we observed its distribution in airway epithelial cells of adult trachea by immunofluorescence (IF) microscopy, using samples fixed with paraformaldehyde (PFA). The results showed that CAMSAP3 was concentrated around the apical plasma membranes (Fig. 3A), as assessed by co-immunostaining for EZRIN, which is known to

associate with the apical membranes or microvilli (Berryman et al., 1993), as observed in other epithelial cells (Kimura et al., 2021; Robinson et al., 2020; Toya et al., 2016; Usami et al., 2021). This position of CAMSAP3 corresponded to the proximal edge of strong α-tubulin IF signals that should represent ciliary microtubules (Fig. 3A). Weak CAMSAP3 IF stains were also detectable along cilia as well as in the cytoplasm. We then examined airway epithelia of *Camsap3*$^{dc/dc}$ mice and found that mutant CAMSAP3 molecules (CKK domain-truncated CAMSAP3) also accumulated at the apical zones, overlapping with EZRIN (Fig. 3B). Curiously, the relative intensity of IF signal for the mutant CAMSAP3 increased in the cilia, compared to the wild-type samples, suggesting that the mutant CAMSAP3, which is not capable of binding to microtubules, penetrates into the cilia more readily than the wild-type CAMSAP3.

Localization of CAMSAP3 at three distinct sites

To gain more detailed information on CAMSAP3 localization in the cilia and basal bodies, we co-immunostained CAMSAP3 and components of the cilium-basal body complex, analyzing their IF images by Airyscan confocal laser-scanning microscopy, which provides super-resolution images. For this experiment, we used methanol for fixation of tissues, since some of the proteins to be examined did not give reproducible IF signals in PFA-fixed specimens. The analysis first revealed that CAMSAP3 IF signals, which are condensed at the apical zone of a cell, were split into at least three rows of CAMSAP3 puncta designated #1, #2 and #3 (Fig. 4A). Additional puncta were also detectable outside the three rows, but their presence or location was variable. Individual CAMSAP3 puncta comprising the three rows were also aligned along the apicobasal axis of the cell, likely due to their association with a single cilium-basal body

complex at different levels of the apicobasal axis. Occasionally, this alignment of the three CAMSAP3 puncta along the apicobasal axis was disrupted in various ways, but it remains to be determined whether this was an intrinsic event or artificially produced during sample preparation.

We then detected microtubules by α-tubulin immunostaining (Fig. 4A, leftmost). Cytoplasmic microtubules formed meshwork below the #3 row of CAMSAP3 puncta, and some of them entered into the #3 zone of CAMSAP3, yielding their overlapping view. On the other hand, ciliary microtubules, which should have a structural continuity to the basal body, were not clearly detectable at their proximal regions in our methanol-fixed samples for unknown reasons. Nevertheless, CAMSAP3 puncta at the #1 row exhibited some overlapping with microtubule clusters.

To determine the structural relationship between CAMSAP3 and basal body, we co-immunostained for CAMSAP3 and Odf2 which is known to localize at the transition fibers and basal feet (Kunimoto et al., 2012). Odf2 overlapped with CAMSAP3 puncta only at their #3 row, further extending down to CAMSAP3-negative zones (Fig. 4A middle). We also examined the distribution of γ-tubulin, which has been reported to accumulate at the basal foot or nearby positions (Clare et al., 2014; Hagiwara et al., 2000). γ-Tubulin was detected as a clear punctate IF signal that is located below the #3 row of CAMSAP3 puncta (Fig. 4A rightmost).

We next analyzed the distribution of the CKK domain-truncated CAMSAP3 by Airyscan microscopy in *Camsap3*$^{dc/dc}$ cells (Fig. 4B). As seen for wild-type CAMSAP3,

the mutant molecules formed multiple rows. Co-immunostaining for CAMSAP3 and microtubules, Odf2, or γ-tubulin showed that their spatial relationships were similar to those found in wild-type cells. However, we could not convincingly detect the #1 row, although CAMSAP3 IF signals were randomly present at the ciliary zone (Fig. 4B), consistent with the results obtained using PFA-fixed samples. We also noted that CAMSAP3 puncta in the #2 row were missing in places. These suggest that, although the mutated CAMSAP3 still associates with the cilium-basal body system at the #3 site, it does not do so at the #1 site, and the #2 site appeared to be an intermediate situation.

Top row of CAMSAP3 puncta localizes at an upper transition zone

To further confirm the localization of CAMSAP3, we prepared transverse sections of a wild-type ciliated cell and detected Odf2 using STED microscopy, which can visualize its circular distribution in super-resolution (Fig. 5A). By moving the focus up and down along the apicobasal axis, we confirmed the presence of CAMSAP3 puncta above and also around the Odf2-positive zone (Movie 5). From these observations and the reported localization of Odf2 (Kunimoto et al., 2012), we conclude that the #1 and #2 CAMSAP3 puncta localize at regions above the basal body, whereas the #3 punctum associates with the apical half of the basal body where Odf2 is present (Fig. 5B).

For more precise localization of the #1 and #2 CAMSAP3 puncta, we co-immunostained wild-type ciliated cells for CAMSAP3 and Chibby, a protein that localizes at a proximal region of TZ, playing a role in ciliogenesis (Burke et al., 2014; Enjolras et al., 2012). Confocal microscopy of longitudinal sections first showed that Chibby localizes between the #1 and #2 CAMSAP3 puncta with some overlapping (Fig.

5C). Then, we analyzed transverse sections using STED microscopy to detect Chibby, which gave a circular image of this protein distribution, consistent with a previous report (Burke et al., 2014). Continuous optical sections showed that, while CAMSAP3 overlaps with Chibby at some levels, it also localizes at the levels above Chibby (Fig. 5D and Movie 6), which confirmed the results obtained by longitudinal sections. Given that Chibby accumulates at a proximal TZ, our results suggest that the #1 CAMSAP3 puncta are localized at a distal portion of TZ or at BP that is contiguous to TZ, while #2 is around the border between TZ and basal body, as summarized in Fig. 5B.

Finally, we viewed the overall distribution pattern of basal bodies and microtubules from the top of ciliated cells in which GFP-tagged Centrin 2, a basal body protein, is genetically expressed (Higginbotham et al., 2004). Basal bodies exhibited typical horizontal arrays in wild-type cells, and a similar pattern was maintained in *Camsap3*-mutated cells (Fig. 6). Microtubules form a horizontal network at the inter-basal body spaces (Kunimoto et al., 2012; Tateishi et al., 2017; Tateishi et al., 2013), and we did not find any particular change of this network in *Camsap3*-mutated cells (Fig. 6, and Movies 7 and 8). Microtubules located below the basal bodies also formed networks, and their pattern was indistinguishable between wild-type and *Camsap3*-mutated cells. Thus, it seems that *Camsap3* mutation did not affect the overall basal body assembly, nor the horizontal networks of microtubules associated with the basal bodies.

Discussion

The present study demonstrated that CAMSAP3 concentrates at multiple sites of the cilium-basal body complex, and dysfunction of this molecule results in unsynchronized beating of multicilia, as well as the loss of CP and other structural defects in this complex. A preceding study using nasal epithelial cells reported that a *Camsap3* hypomorphic mutation caused similar functional and structural defects in the multicilia, and CAMSAP3 formed a single dot between the axoneme and basal body in mature adult mice (Robinson et al., 2020). Our super-resolution microscopic analysis revealed that the CAMSAP3-bearing region is subdivided into three distinct sites: upper (#1) and lower (#2) sites of TZ, and an upper site of the basal body (#3) in airway multiciliated cells of trachea (Fig. 5B). This enables us to study the function of this molecule at higher structural resolutions.

CAMSAP3 binds the minus-end of a microtubule, stabilizing it, and simultaneously serves to tether the microtubule filament to particular subcellular sits (Nashchekin et al., 2016; Toya et al., 2016). From these established functions of CAMSAP3 as well as the observed localization of CAMSAP3 at the #1 site which corresponds to the upper TZ or the BP contiguous to TZ, we can infer that CAMSAP3 may regulate the stability of CP or its anchoring to the basal plate through their interactions, as the minus ends of axonemal microtubules are oriented basally (Euteneuer and Mcintosh, 1981). Removal of this potential function of CAMSAP3 would have led to a collapse of the CP. Intriguingly, the CKK-truncated CAMSAP3 expressed in *Camsap3*$^{dc/dc}$ mice, which is unable to bind the minus-ends of microtubules, was not clustered at the #1 site. This observation accords with the idea that CAMSAP3 interacts with the CP via the CKK domain, as it has been shown that CAMSAP3 requires CKK-dependent interaction with

microtubules for displaying a clustered appearance in certain epithelial cells (Tanaka et al., 2012; Toya et al., 2016). On the other hand, the CKK-deficient CAMSAP3 puncta were still detectable at the #3 site (and also partly at the #2 site) of airway cells, as observed in some other tissues (Kimura et al., 2021; Mitsuhata et al., 2021), implying the possibility that CAMSAP3 is able to cluster independently of microtubules, when it binds particular subcellular structures or molecules.

BP architecture was also perturbed to some extent in *Camsap3*-mutated airway cells, which suggests that CAMSAP3 may serve as a regulator of the basal plate, as well. We additionally noted the presence of low levels of CAMSAP3 throughout a cilium, and its density appeared to have increased in *Camsap3*-mutated cilia, hinting at some potential function of CAMSAP3 within the main body of a cilium. To test this possibility, however, we will need additional studies.

How the basal body polarity was perturbed in the absence of functional CAMSAP3 also remains to be investigated. CAMSAP3 at the #2 and #3 sites could have some role in determining the basal body polarity. It is also possible that the aberrant beating of multicilia in *Camsap3*-mutated cells cannot produce sufficient hydrodynamic forces that are required for the polarized alignment of them (Guirao et al., 2010). On the other hand, the horizontal microtubule networks that are present at the level of or below the basal bodies were apparently not affected by *Camsap3* mutation, which suggests that their assembly is regulated by factors other than CAMSAP3, such as γ-tubulin, an authentic microtubule nucleator. Which defects in the cilium-basal body complex observed in *Camsap3*-mutated cells primarily produced unsynchronized beating of cilia

remains undetermined, but it is likely that both the axonemal abnormalities and disrupted basal body polarity were involved in this process.

Curiously, the role of CAMSAP3 in the multiciliary system appears not thoroughly conserved among the multiciliated cells from different organs. For example, the CP was not particularly missing in multiciliated cells of the oviducts from the *Camsap3*$^{dc/dc}$ mice (Usami et al., 2021), although these cells showed a defect in the basal body polarity, as observed in airway epithelial cells. More surprisingly, in multiciliated ependymal cells of the brain, CAMSAP3 does not associate with the cilium-basal body complex, and their ciliary beating occurs normally in *Camsap3*-mutant mice (Kimura et al., 2021). In the ependymal cells, CAMSAP3 localizes under the apical plasma membranes and its major role is to regulate the organization of cortical microtubules that are required for establishing a microtubule-dependent signaling system. These observations suggest that CAMSAP3 contributes to multicilia organization in a tissue-specific manner, although the possibility that other CAMSAP subtypes or unidentified similar proteins have taken over the role of CAMSAP3 in the oviduct and ependymal cells is not excluded. Future studies will be necessary to reveal how CAMSAP3 becomes associated with the cilium-basal body complex and regulates its structure and function only in particular tissues.

Materials and Methods

Mice

A *Camsap3* mutant mouse line, *Camsap3*$^{dc/dc}$, was described previously (Toya et al., 2016). The transgenic mouse line expressing GFP-Centrin2 (EGFP-CETN2) was a gift from Holden Higginbotham, Brigham Young University (Higginbotham et al., 2004). Female mice of this transgenic line were crossed with *Camsap3*$^{dc/+}$ males to generate those expressing GFP-Centrin2 under *Camsap3* mutation. ICR mice (Slc; ICR, Japan SLC) were used to for immunostaining analysis of Chibby. The age of mice used for the study was recorded for each experiment and described in the legends of figures. The experiments using mice were performed in accordance with the protocol(s) approved by the Institutional Animal Care and Use Committee of the RIKEN Center for Biosystems Dynamics Research (RIKEN Kobe Branch), or the Guidelines of Animal Experimentation of National Institutes for Natural Sciences.

Scanning electron microscopy

Mice were anesthetized with isoflurane, and dissected to reveal trachea and cut diaphragm. The tracheas were prefixed with a fixative solution (2% paraformaldehyde and 2.5% glutaraldehyde in 0.1M cacodylate buffer, pH 7.4) for 5 min, then removed from mice. The trachea was cut into small pieces, and the samples were immersed in the same fixative solution at room temperature for 2 hr. The samples were washed with 0.1M cacodylate buffer and postfixed in 1% OsO4 in 0.1M cacodylate buffer on ice for 2 hr. Then the samples were washed with distilled water, and stained overnight with 0.5% aqueous uranyl acetate at room temperature. The stained samples were dehydrated with ethanol the samples were rinsed with distilled water, and further stained with 0.5% uranyl acetate solution overnight at room temperature. The samples were rinsed with distilled water and dehydrated through a graded series of ethanol, transferred to

isopentyl acetate and critical point-dried using liquid CO_2. The dried specimens were evaporation-coated with Osmium and examined in a JSM-5600LV scanning electron microscope at an accelerating voltage of 10 kV.

Transmission electron microscopy

Tracheas were fixed with 2% paraformaldehyde and 2.5% glutaraldehyde in 0.1M cacodylate buffer (pH 7.4) at 4°C overnight. After washing five times with 0.1M cacodylate buffer, the specimens were further fixed with 1% OsO4 in 0.1M cacodylate buffer at 4°C for 1 h and then washed five times with Milli-Q water. The specimens were incubated in 1% uranyl acetate overnight and washed five times with Milli-Q water. Specimens were dehydrated with ethanol series (20%, 50%, 70%, 90% and 99.5% for 5 min each, and twice in 100% for 10 min) and acetone, then followed by infiltration with Epon 812 (TAAB). Polymerization was performed at 60°C for 72 h. Samples were cut with an ultramicrotome (ULTRA CUT UCT, Leica) equipped with a diamond knife (Diatome), doubly stained with uranyl acetate and lead citrate, and examined in a transmission electron microscope (JEM-1400 Plus ; JEOL) operated at 100 kV.

Immunofluorescence staining and microscopy

Isolated trachea tissue was fixed in a PEM buffer (PEM: 100 mM PIPES, 5 mM EGTA, and 5 mM $MgCl_2$, adjusted to pH 6.9 with 2 M KOH) containing 2% paraformaldehyde and 0.1 M sorbitol for 1 h at room temperature, except that the tissue was treated with 4% paraformaldehyde at 37°C for 1 hr and then at 4°C for 24 hr for microtubule fixation. Alternatively, trachea tissue was fixed with methanol for 20 to 45 min at –

20°C, followed by treatment with acetone for 1 min at –20°C. After fixation, the tissue was rinsed three times with PEM for 10 min. Then, cryoprotection was carried out by incubation with 15% sucrose in PEM overnight at 4°C, followed by incubation with 20% sucrose in PEM for 6 h, and 30% sucrose in PEM overnight at 4°C. The tissue was frozen in OCT compound in an embedding mold (Polysciences, Inc.) in liquid nitrogen and stored at –80°C. Frozen samples were sliced at 7 mm thickness with a cryostat (HM500M, MICROM).

After washing twice with PBS, the sections were blocked with Blocking One (Nacalai Tesque) for 1 hr at room temperature, followed by incubation with primary antibodies in Blocking One (Nacalai Tesque) overnight at 4ºC. Sections were washed two times with PBS and incubated for one hour at RT with corresponding secondary antibodies. Stained sections were washed two times with PBS and mounted with either Fluorsave (Chemicon) or 2,2′-thiodiethanol (Staudt et al., 2007). For some samples, antigen retrieval was performed by incubating sections in HistoVT One (Nacalai Tesque) for 3 min at 95ºC, prior to the incubation with primary antibodies.

For conventional immunofluorescence microscopy, samples were analyzed by Zeiss Axiopan 2 through Plan-APOCHROMAT 63x/1.4 Oil Dic or Plan-NEOFLUAR 40x/1.3 Oil Dic objectives. For confocal microscopy, a NIKON A1 microscope with Nikon Plan Apo Vc 100x/1.40 oil OFN25 DIC N2 objective lens was used. For super-resolution microscopy, stacks of images were taken along the z-axis at optimal intervals using Airyscan (LSM880, Zeiss) with 63x/1.40 NA and a 100x/1.46 NA objective lenses. TCS SP8 STED with HCX PL APO CS 100x/1.40 oil immersion objective lens

(Leica) was used to acquire the horizontal views of cells, and the optical conditions for this imaging are shown in Supplementary Table 1. Acquired images were processed using Zen (Zeiss), Adobe Photoshop (Adobe), or ImageJ (Wayne Rasband, NIH).

Live imaging of ciliary motion and quantification of data

Live images of cilia were acquired as described previously (Shinohara et al., 2015). Briefly, tracheas were collected into HEPES-buffered Dulbecco's modified Eagle's medium (pH7.2) supplemented with 10% fetal bovine serum. Motility of cilia was examined at 25°C with a high-speed CMOS camera (HAS-U2, DITECT) that was connected to a microscope (BX53, Olympus) with a 40x objective lens (UPLFLN40X, Olympus) at a frame rate of 300 frames/s for tracheal cilia. To emphasize the movement of cilia, time-series images were adjusted to gain proper contrast and brightness after subtracting the minimum value through the images from each frame using ImageJ.

The synchrony of the motion of the cilia was quantified by calculating the flow field of the cilia carpet by PIV analysis. We denoised the time-lapse images (128 pix x 128 pix) by a Gaussian filter followed by the enhancement of the contrast using Fiji plugins. Then, the flow field of the time-lapse images was obtained by PIV analysis using a python library (OpenPIV). The interrogation window of PIV was 32 pix, and the overlap between adjacent interrogation areas was 24 pix.

Antibodies

The following primary antibodies were used: Rabbit anti-CAMSAP3 (Tanaka et al., 2012, 1: 100), mouse anti-α-tubulin (clone DM1A, Sigma-Aldrich T9026, 1:1000),

rabbit monoclonal anti-β-tubulin (clone 9F3, Cell Signaling Technology Cat#2128, 1: 100), mouse anti-γ-tubulin (Sigma-Aldrich T6557, 1:1000), rabbit anti-γ-tubulin (Sigma-Aldrich T3559, 1:500), mouse anti-EZRIN (Abcam 4069, 1:100), rat anti-Odf2 (a gift from Sachiko Tsukita, Osaka University, 1: 2), mouse monoclonal anti-Chibby (Santa Cruz sc-101551, 1:100). The following secondary antibodies were used: Donkey CF-488A anti-rat IgG (Biotium 20027, 1:000) and CF-568 anti-rabbit IgG (Biotium 20698, 1:1000) antibodies; goat Alexa Fluor-488 anti-rat IgG (Invitrogen, A-11006, 1:500), Alexa Fluor-488 anti-rabbit IgG (Invitrogen, A-11034, 1:500), Alexa Fluor-568 anti-mouse IgG (Invitrogen, A-11031, 1:500), Alexa Fluor-594 anti-rabbit IgG (Invitrogen A-11037, 1:500), Alexa Fluor-647 anti-rabbit IgG (Invitrogen, A-21245, 1:500) and Alexa Fluor-647 anti-mouse IgG (Invitrogen, A-21236, 1:1000) antibodies; and goat STAR580 anti-mouse IgG (Abberior 2-0002-005-1, 1:500) and STAR635P anti-rat IgG (Abberior 2-0132-007-5, 1:500).

Audio recording

Respiratory sound of mice was recorded using the Voice Memos application installed in iPhone XS (Apple).

Acknowledgements

We thank Hiroshi Hamada for his support of live imaging experiments, and Mitsuru Morimoto for his advice on the study of lung, Sachiko Tsukita for anti-Odf2 antibody, and Ritsu Kamiya for critical reading of the manuscript. This work was supported by the program Grant-in-Aid for Scientific Research (S) (grant number 25221104) from the

Japan Society for Promotion of Science to M.Ta; and by the Japan Society for the Promotion of Science, KAKENHI (grant numbers 17H03689 and 16H06280) and the Japan Science and Technology Agency, Core Research for Evolutional Science and Technology (JPMJCR1654) to T.F.

Author contributions

Conceptualization: M.Ta., M.To.; Formal analysis: T.Y., T.S.; Investigation: H.S., F.M-U., T.K., T.I., K.O., S.O., K.M., M.To.; Writing-original draft: M.Ta.; Writing-reviews & editing: M.To., T.F., F.M-U.; Supervision: M.Ta., T.F., S.Y.; Project administration: M.Ta.; Funding acquisition: M.Ta., T.F.

References

Baines, A.J., P.A. Bignone, M.D. King, A.M. Maggs, P.M. Bennett, J.C. Pinder, and G.W. Phillips. 2009. The CKK domain (DUF1781) binds microtubules and defines the CAMSAP/ssp4 family of animal proteins. *Molecular biology and evolution*. 26:2005-2014.

Bautista-Harris, G., G. Julia-Serda, F. Rodriguez de Castro, I. Santana-Benitez, and P. Cabrera-Navarro. 2000. Absence of central microtubules and transposition in the ciliary apparatus of three siblings. *Respiration*. 67:449-452.

Berryman, M., Z. Franck, and A. Bretscher. 1993. Ezrin is concentrated in the apical microvilli of a wide variety of epithelial cells whereas moesin is found primarily in endothelial cells. *J Cell Sci*. 105 (Pt 4):1025-1043.

Brooks, E.R., and J.B. Wallingford. 2014. Multiciliated cells. *Curr Biol*. 24:R973-982.

Burgoyne, T., A. Lewis, A. Dewar, P. Luther, C. Hogg, A. Shoemark, and M. Dixon. 2014. Characterizing the ultrastructure of primary ciliary dyskinesia transposition defect using electron tomography. *Cytoskeleton (Hoboken)*. 71:294-301.

Burke, M.C., F.Q. Li, B. Cyge, T. Arashiro, H.M. Brechbuhl, X. Chen, S.S. Siller, M.A. Weiss, C.B. O'Connell, D. Love, C.J. Westlake, S.D. Reynolds, R. Kuriyama, and K. Takemaru. 2014. Chibby promotes ciliary vesicle formation and basal body docking during airway cell differentiation. *J Cell Biol*. 207:123-137.

Chen, Y., J. Zheng, X. Li, L. Zhu, Z. Shao, X. Yan, and X. Zhu. 2020. Wdr47 Controls Neuronal Polarization through the Camsap Family Microtubule Minus-End-Binding Proteins. *Cell Rep*. 31:107526.

Chuang, M., A. Goncharov, S. Wang, K. Oegema, Y. Jin, and A.D. Chisholm. 2014. The microtubule minus-end-binding protein patronin/PTRN-1 is required for axon regeneration in C. elegans. *Cell Rep*. 9:874-883.

Clare, D.K., J. Magescas, T. Piolot, M. Dumoux, C. Vesque, E. Pichard, T. Dang, B. Duvauchelle, F. Poirier, and D. Delacour. 2014. Basal foot MTOC organizes pillar MTs required for coordination of beating cilia. *Nat Commun*. 5:4888.

Czarnecki, P.G., and J.V. Shah. 2012. The ciliary transition zone: from morphology and molecules to medicine. *Trends Cell Biol*. 22:201-210.

Damseh, N., N. Quercia, N. Rumman, S.D. Dell, and R.H. Kim. 2017. Primary ciliary dyskinesia: mechanisms and management. *Appl Clin Genet*. 10:67-74.

Dawe, H.R., H. Farr, and K. Gull. 2007a. Centriole/basal body morphogenesis and migration during ciliogenesis in animal cells. *J Cell Sci*. 120:7-15.

Dawe, H.R., M.K. Shaw, H. Farr, and K. Gull. 2007b. The hydrocephalus inducing gene product, Hydin, positions axonemal central pair microtubules. *BMC Biol*. 5:33.

Dean, S., F. Moreira-Leite, V. Varga, and K. Gull. 2016. Cilium transition zone proteome reveals compartmentalization and differential dynamics of ciliopathy complexes. *Proc Natl Acad Sci U S A*. 113:E5135-5143.

Dute, R., and C. Kung. 1978. Ultrastructure of the proximal region of somatic cilia in Paramecium tetraurelia. *J Cell Biol*. 78:451-464.

Enjolras, C., J. Thomas, B. Chhin, E. Cortier, J.L. Duteyrat, F. Soulavie, M.J. Kernan, A. Laurencon, and B. Durand. 2012. Drosophila chibby is required for basal body formation and ciliogenesis but not for Wg signaling. *J Cell Biol*. 197:313-325.

Euteneuer, U., and J.R. Mcintosh. 1981. Polarity of Some Motility-Related Microtubules. *P Natl Acad Sci-Biol*. 78:372-376.

Feng, C., P. Thyagarajan, M. Shorey, D.Y. Seebold, A.T. Weiner, R.M. Albertson, K.S. Rao, A. Sagasti, D.J. Goetschius, and M.M. Rolls. 2019. Patronin-mediated minus end growth is required for dendritic microtubule polarity. *J Cell Biol*. 218:2309-2328.

Gilula, N.B., and P. Satir. 1972. The ciliary necklace. A ciliary membrane specialization. *J Cell Biol*. 53:494-509.

Goncalves, J., and L. Pelletier. 2017. The Ciliary Transition Zone: Finding the Pieces and Assembling the Gate. *Mol Cells*. 40:243-253.

Goodwin, S.S., and R.D. Vale. 2010. Patronin Regulates the Microtubule Network by Protecting Microtubule Minus Ends. *Cell*. 143:263-274.

Greenan, G.A., R.D. Vale, and D.A. Agard. 2020. Electron cryotomography of intact motile cilia defines the basal body to axoneme transition. *J Cell Biol*. 219.

Guirao, B., A. Meunier, S. Mortaud, A. Aguilar, J.M. Corsi, L. Strehl, Y. Hirota, A. Desoeuvre, C. Boutin, Y.G. Han, Z. Mirzadeh, H. Cremer, M. Montcouquiol, K. Sawamoto, and N. Spassky. 2010. Coupling between hydrodynamic forces and planar cell polarity orients mammalian motile cilia. *Nat Cell Biol*. 12:341-350.

Hagiwara, H., A. Kano, T. Aoki, N. Ohwada, and K. Takata. 2000. Localization of gamma-tubulin to the basal foot associated with the basal body extending a cilium. *Histochem J*. 32:669-671.

Hendershott, M.C., and R.D. Vale. 2014. Regulation of microtubule minus-end dynamics by CAMSAPs and Patronin. *Proc Natl Acad Sci U S A*. 111:5860-5865.

Higginbotham, H., S. Bielas, T. Tanaka, and J.G. Gleeson. 2004. Transgenic mouse line with green-fluorescent protein-labeled Centrin 2 allows visualization of the centrosome in living cells. *Transgenic Res*. 13:155-164.

Hoog, J.L., S. Lacomble, E.T. O'Toole, A. Hoenger, J.R. McIntosh, and K. Gull. 2014. Modes of flagellar assembly in Chlamydomonas reinhardtii and Trypanosoma brucei. *Elife*. 3:e01479.

Jiang, K., S. Hua, R. Mohan, I. Grigoriev, K.W. Yau, Q. Liu, E.A. Katrukha, A.F. Altelaar, A.J. Heck, C.C. Hoogenraad, and A. Akhmanova. 2014. Microtubule minus-end stabilization by polymerization-driven CAMSAP deposition. *Dev Cell*. 28:295-309.

Kimura, T., H. Saito, M. Kawasaki, and M. Takeichi. 2021. CAMSAP3 is required for mTORC1-dependent ependymal cell growth and lateral ventricle shaping in mouse brains. *Development*. 148.

King, M.D., G.W. Phillips, P.A. Bignone, N.V. Hayes, J.C. Pinder, and A.J. Baines. 2014. A conserved sequence in calmodulin regulated spectrin-associated protein 1 links its interaction with spectrin and calmodulin to neurite outgrowth. *J Neurochem*. 128:391-402.

Ko, C.S., V. Tserunyan, and A.C. Martin. 2019. Microtubules promote intercellular contractile force transmission during tissue folding. *J Cell Biol*. 218:2726-2742.

Kunimoto, K., Y. Yamazaki, T. Nishida, K. Shinohara, H. Ishikawa, T. Hasegawa, T. Okanoue, H. Hamada, T. Noda, A. Tamura, S. Tsukita, and S. Tsukita. 2012. Coordinated ciliary beating requires Odf2-mediated polarization of basal bodies via basal feet. *Cell*. 148:189-200.

Lechtreck, K.F., P. Delmotte, M.L. Robinson, M.J. Sanderson, and G.B. Witman. 2008. Mutations in Hydin impair ciliary motility in mice. *J Cell Biol*. 180:633-643.

Lee, L. 2011. Mechanisms of mammalian ciliary motility: Insights from primary ciliary dyskinesia genetics. *Gene*. 473:57-66.

Loreng, T.D., and E.F. Smith. 2017. The Central Apparatus of Cilia and Eukaryotic Flagella. *Cold Spring Harb Perspect Biol*. 9.

Martin, M., A. Veloso, J. Wu, E.A. Katrukha, and A. Akhmanova. 2018. Control of endothelial cell polarity and sprouting angiogenesis by non-centrosomal microtubules. *Elife*. 7.

Meng, W., Y. Mushika, T. Ichii, and M. Takeichi. 2008. Anchorage of microtubule minus ends to adherens junctions regulates epithelial cell-cell contacts. *Cell*. 135:948-959.

Mitsuhata, Y., T. Abe, K. Misaki, Y. Nakajima, K. Kiriya, M. Kawasaki, H. Kiyonari, M. Takeichi, M. Toya, and M. Sato. 2021. Cyst formation in proximal renal tubules caused by dysfunction of the microtubule minus-end regulator CAMSAP3. *Sci Rep*. 11:5857.

Nashchekin, D., A.R. Fernandes, and D. St Johnston. 2016. Patronin/Shot Cortical Foci Assemble the Noncentrosomal Microtubule Array that Specifies the Drosophila Anterior-Posterior Axis. *Dev Cell*. 38:61-72.

Noordstra, I., Q. Liu, W. Nijenhuis, S. Hua, K. Jiang, M. Baars, S. Remmelzwaal, M. Martin, L.C. Kapitein, and A. Akhmanova. 2016. Control of apico-basal epithelial polarity by the microtubule minus-end-binding protein CAMSAP3 and spectraplakin ACF7. *J Cell Sci*. 129:4278-4288.

Nozawa, Y.I., E. Yao, C. Lin, J.H. Yang, C.W. Wilson, R. Gacayan, and P.T. Chuang. 2013. Fused (Stk36) is a ciliary protein required for central pair assembly and motile cilia orientation in the mammalian oviduct. *Dev Dyn*. 242:1307-1319.

Pongrakhananon, V., H. Saito, S. Hiver, T. Abe, G. Shioi, W. Meng, and M. Takeichi. 2018. CAMSAP3 maintains neuronal polarity through regulation of microtubule stability. *Proc Natl Acad Sci U S A*. 115:9750-9755.

Richardson, C.E., K.A. Spilker, J.G. Cueva, J. Perrino, M.B. Goodman, and K. Shen. 2014. PTRN-1, a microtubule minus end-binding CAMSAP homolog, promotes microtubule function in Caenorhabditis elegans neurons. *Elife*. 3:e01498.

Robinson, A.M., S. Takahashi, E.J. Brotslaw, A. Ahmad, E. Ferrer, D. Procissi, C.P. Richter, M.A. Cheatham, B.J. Mitchell, and J. Zheng. 2020. CAMSAP3 facilitates basal body polarity and the formation of the central pair of microtubules in motile cilia. *Proc Natl Acad Sci U S A*. 117:13571-13579.

Satir, P., and S.T. Christensen. 2007. Overview of structure and function of mammalian cilia. *Annu Rev Physiol*. 69:377-400.

Shinohara, K., D. Chen, T. Nishida, K. Misaki, S. Yonemura, and H. Hamada. 2015. Absence of Radial Spokes in Mouse Node Cilia Is Required for Rotational Movement but Confers Ultrastructural Instability as a Trade-Off. *Dev Cell*. 35:236-246.

Smith, E.F., and P. Yang. 2004. The radial spokes and central apparatus: mechano-chemical transducers that regulate flagellar motility. *Cell Motil Cytoskeleton*. 57:8-17.

Stannard, W., A. Rutman, C. Wallis, and C. O'Callaghan. 2004. Central microtubular agenesis causing primary ciliary dyskinesia. *Am J Respir Crit Care Med*. 169:634-637.

Staudt, T., M.C. Lang, R. Medda, J. Engelhardt, and S.W. Hell. 2007. 2,2'-thiodiethanol: a new water soluble mounting medium for high resolution optical microscopy. *Microsc Res Tech*. 70:1-9.

Takeda, M., M.M. Sami, and Y.C. Wang. 2018. A homeostatic apical microtubule network shortens cells for epithelial folding via a basal polarity shift. *Nat Cell Biol*. 20:36-45.

Tanaka, N., W. Meng, S. Nagae, and M. Takeichi. 2012. Nezha/CAMSAP3 and CAMSAP2 cooperate in epithelial-specific organization of noncentrosomal microtubules. *Proc Natl Acad Sci U S A*. 109:20029-20034.

Tateishi, K., T. Nishida, K. Inoue, and S. Tsukita. 2017. Three-dimensional Organization of Layered Apical Cytoskeletal Networks Associated with Mouse Airway Tissue Development. *Sci Rep*. 7:43783.

Tateishi, K., Y. Yamazaki, T. Nishida, S. Watanabe, K. Kunimoto, H. Ishikawa, and S. Tsukita. 2013. Two appendages homologous between basal bodies and centrioles are formed using distinct Odf2 domains. *J Cell Biol*. 203:417-425.

Tilley, A.E., M.S. Walters, R. Shaykhiev, and R.G. Crystal. 2015. Cilia dysfunction in lung disease. *Annu Rev Physiol*. 77:379-406.

Toya, M., S. Kobayashi, M. Kawasaki, G. Shioi, M. Kaneko, T. Ishiuchi, K. Misaki, W. Meng, and M. Takeichi. 2016. CAMSAP3 orients the apical-to-basal polarity of microtubule arrays in epithelial cells. *Proc Natl Acad Sci U S A*. 113:332-337.

Tucker, J.B. 1971. Development and deployment of cilia, basal bodies, and other microtubular organelles in the cortex of the ciliate Nassula. *J Cell Sci*. 9:539-567.

Usami, F.M., M. Arata, D. Shi, S. Oka, Y. Higuchi, F. Tissir, M. Takeichi, and T. Fujimori. 2021. Intercellular and intracellular cilia orientation is coordinated by CELSR1 and CAMSAP3 in oviduct multi-ciliated cells. *J Cell Sci*. 134.

Wang, Y., M. Rui, Q. Tang, S. Bu, and F. Yu. 2019. Patronin governs minus-end-out orientation of dendritic microtubules to promote dendrite pruning in Drosophila. *Elife*. 8.

Yau, K.W., S.F. van Beuningen, I. Cunha-Ferreira, B.M. Cloin, E.Y. van Battum, L. Will, P. Schatzle, R.P. Tas, J. van Krugten, E.A. Katrukha, K. Jiang, P.S. Wulf, M. Mikhaylova, M. Harterink, R.J. Pasterkamp, A. Akhmanova, L.C. Kapitein,

and C.C. Hoogenraad. 2014. Microtubule minus-end binding protein CAMSAP2 controls axon specification and dendrite development. *Neuron*. 82:1058-1073.

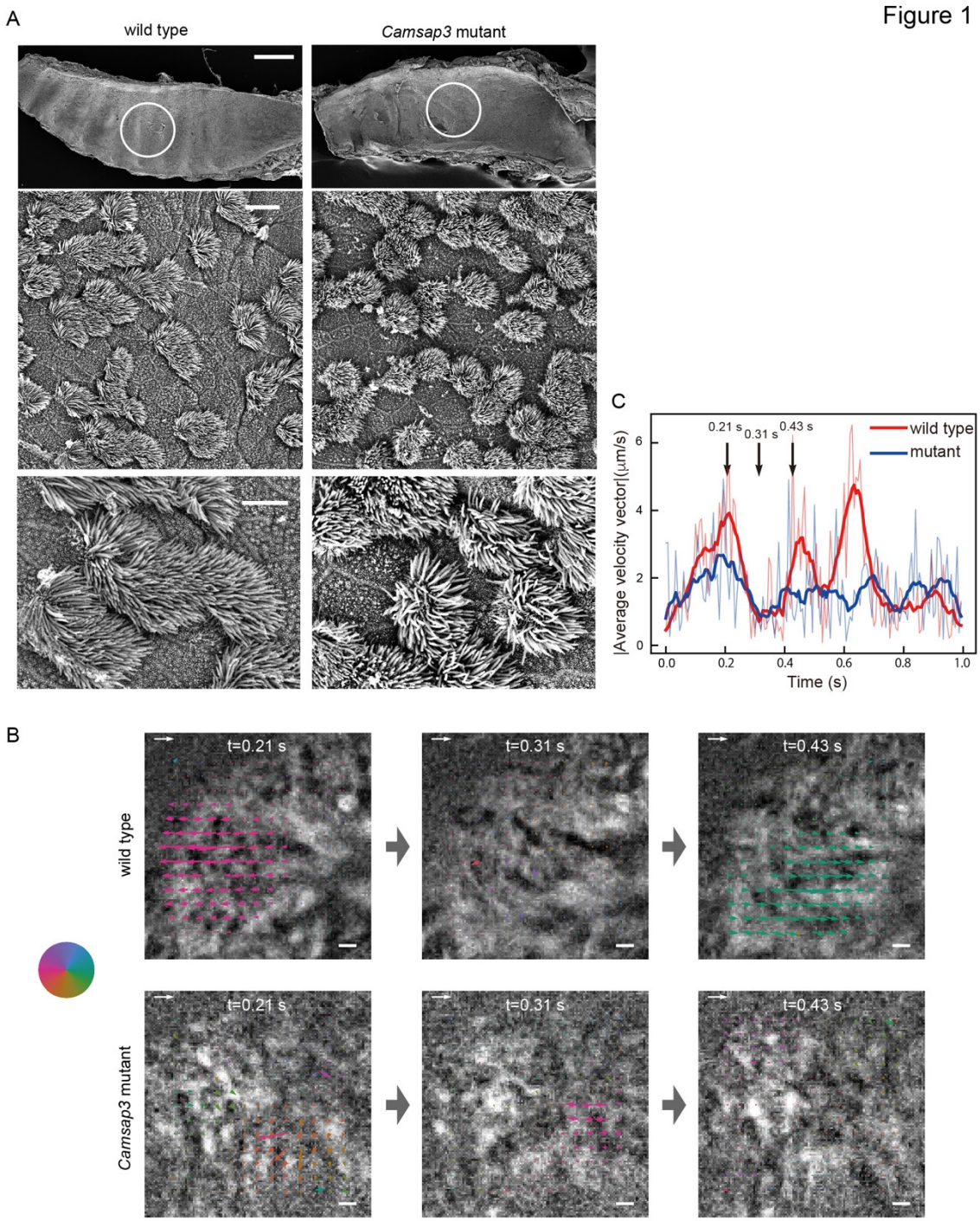

Figure 1. Morphology and time-lapse analysis of cilia in airway epithelial cells.
A. Scanning electron microscopical observation of the luminal surface of trachea. Trachea was isolated from P21 wild-type or *Camsap3* mutant male mice. The top row shows a whole-mount trachea, in which the luminal surface is exposed. Part of the encircled region was enlarged in the middle and bottom rows. Oral side is at the right. Scale bars: 500 μm, top; 10 μm, middle; and 5 μm, bottom.

B. Quantitative analysis of the collective motion of multicilia, which has been recorded in Movies 1 and 2, for a wild-type and *Camsap3*-mutated cell, respectively. These movies were used for PIV analysis (see Movies 3 and 4). Three snapshots, chosen from each movie, are overlaid with the flow vector field calculated by PIV analysis. The vectors represent the velocity vectors. The color of the vectors indicates the angle of the velocity vector, and the colormap is shown as a pie chart. White scale arrow and scale bar on each image are 20 μm/s and 1 μm, respectively.
C. Time-evolution of the magnitude of average velocity vector of ciliary motion plotted for wild-type (red curves) and mutant (blue curves) cells, respectively. The thin curves are the raw data, while the bold curves are the data smoothed by a moving average. The time points shown in B are indicated by black vertical arrows.

Figure 2

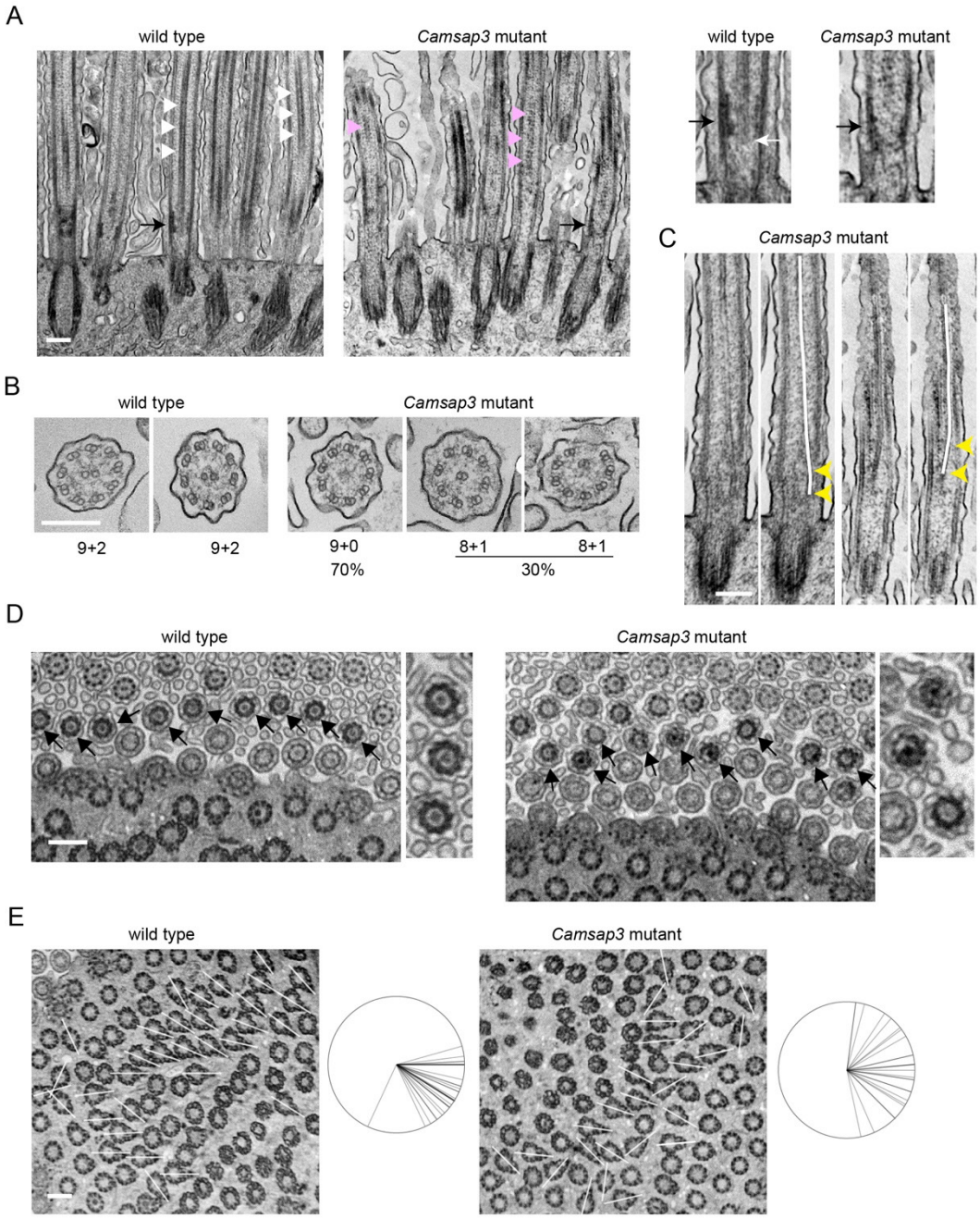

Figure 2. Electron microscopic analysis of cilia and basal bodies.

A. Longitudinal section of a multiciliated cell, which yields a longitudinal view of axonemes and basal bodies. White triangles indicate examples of the CP in a wild-type cell; magenta triangles point to intermittent structures at the central position of axoneme

in a *Camsap3*-mutated cell. Black arrows point to the 'basal plate', and a corresponding position in the *Camsap3* mutant sample. Part of each image is enlarged at the right, in which a white arrow points to the proximal end of the CP. P126 mice were used for every transmission electron microscopic analysis.

B. Transverse section of cilia. In the mutant samples, 218 cilia from two independent sections were used for analysis. The mutant axonemes did not contain a CP, instead some of them had a doublet microtubule that was mislocalized to central or semi-central positions.

C. Longitudinal section of cilia in *Camsap3*-mutated cells. A centrally located microtubule structure tilts toward the peripheral zone at basal portions of axoneme, as indicated by yellow arrowheads. Two examples are shown, each of which is duplicated to trace the central microtubule with a white line over the image.

D. Slightly oblique, transverse sections of a multi-ciliated cell, showing cross-sectional views of axoneme and basal body at various longitudinal levels. Arrows point to axonemes at the level of BP that is characterized by a dense peripheral ring with a central structure. In the mutant section, the BP shows various abnormalities, including loss or over-condensation of the central structure, and partial deformation of the peripheral ring. Part of each image was enlarged and shown after 90° rotation to the right.

E. Slightly oblique, transverse section of a multi-ciliated cell, focusing on the basal foot of basal bodies. The axis of individual basal feet (white bars) is collectively shown at the right of each image. The range of orientation of basal feet on a single cell varied from 26° to 108° in the wild type, with one exceptional case, and 13° to 172° in the mutant sample. 33 and 26 basal bodies were counted for the wild-type and mutant sample, respectively.

Scale bars, 200 nm in A-C; 400 nm in D, E.

Figure 3

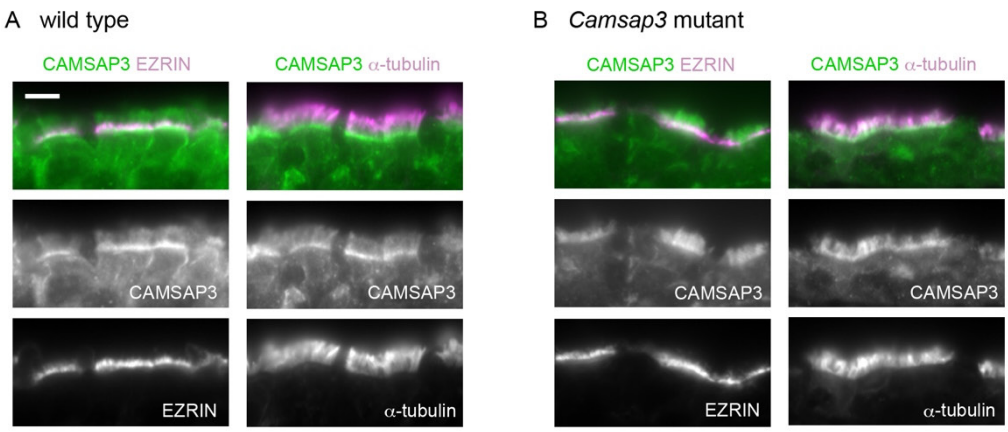

Figure 3. Immunostaining localization of CAMSAP3, EZRIN and α-tubulin. Trachea derived from P176 mice were fixed with 2% PFA, and processed for co-immunostaining for the molecules indicated. Images were recorded by conventional immunofluorescence microscopy. Scale bars, 10 μm.

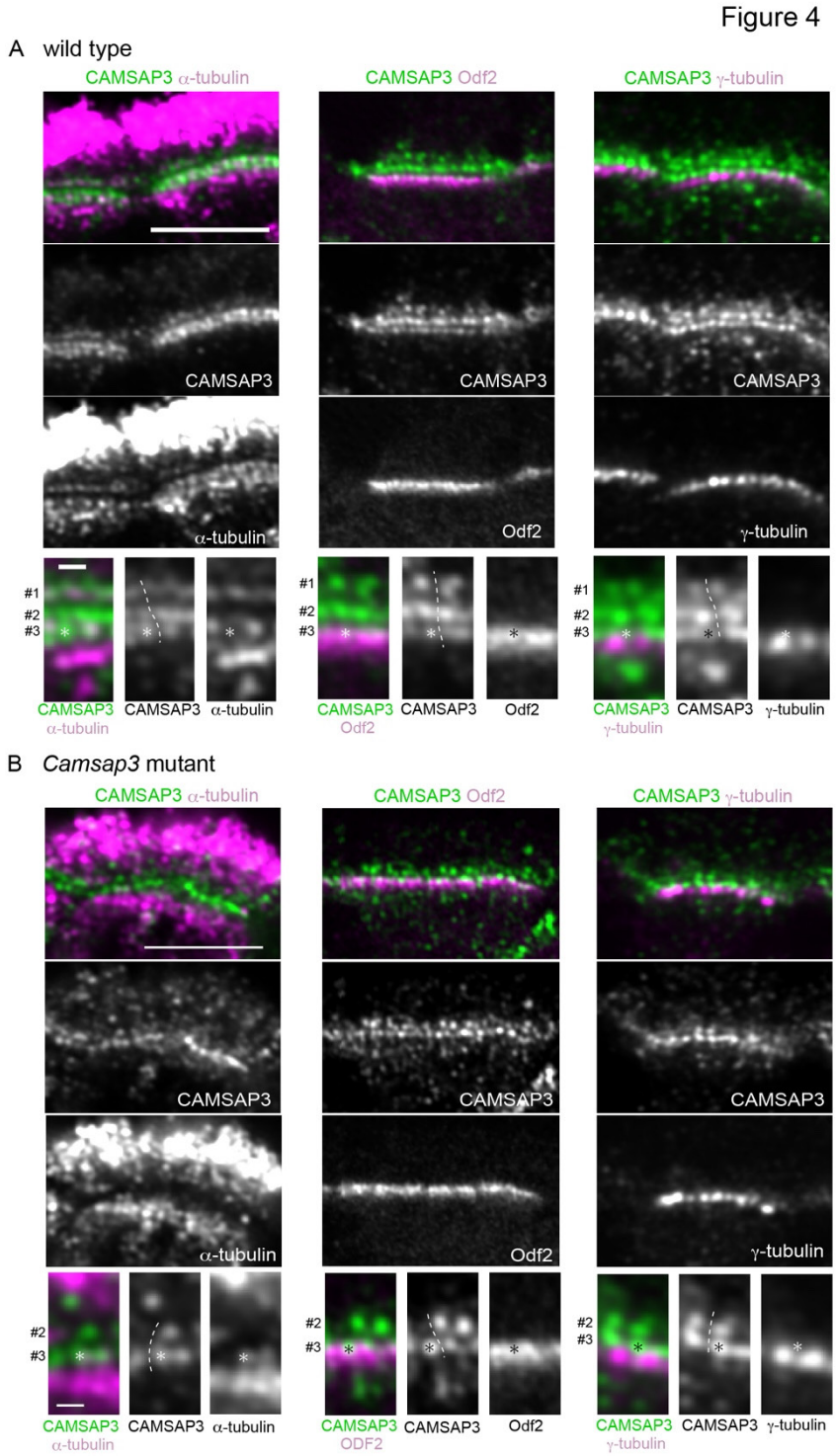

Figure 4. Superresolution microscopical analysis of CAMSAP3 distribution in wild-type and *Camsap3*-mutated multi-ciliated cells.

Vertical views of multi-ciliated cells in wild-type (**A**) or *Camsap3*-mutated (**B**) trachea, which were co-immunostained for the molecules indicated and recorded by Airyscan microscopy. Part of each image was enlarged at the bottom, in which the numbers

indicate three different rows of CAMSAP3 puncta. Asterisks mark an example of CAMSAP3 puncta (or their positions) at the #3 row in each image. Dotted lines indicate a putative boundary between the two sets of CAMSAP3 puncta aligned along the apicobasal axis. The samples were fixed with methanol. P91, P86 and P176 mice were used for immunostaining for α-tubulin, Odf2 and γ-tubulin, respectively.
Scale bars, 5 and 0.5 μm in the original and enlarged images, respectively.

Figure 5

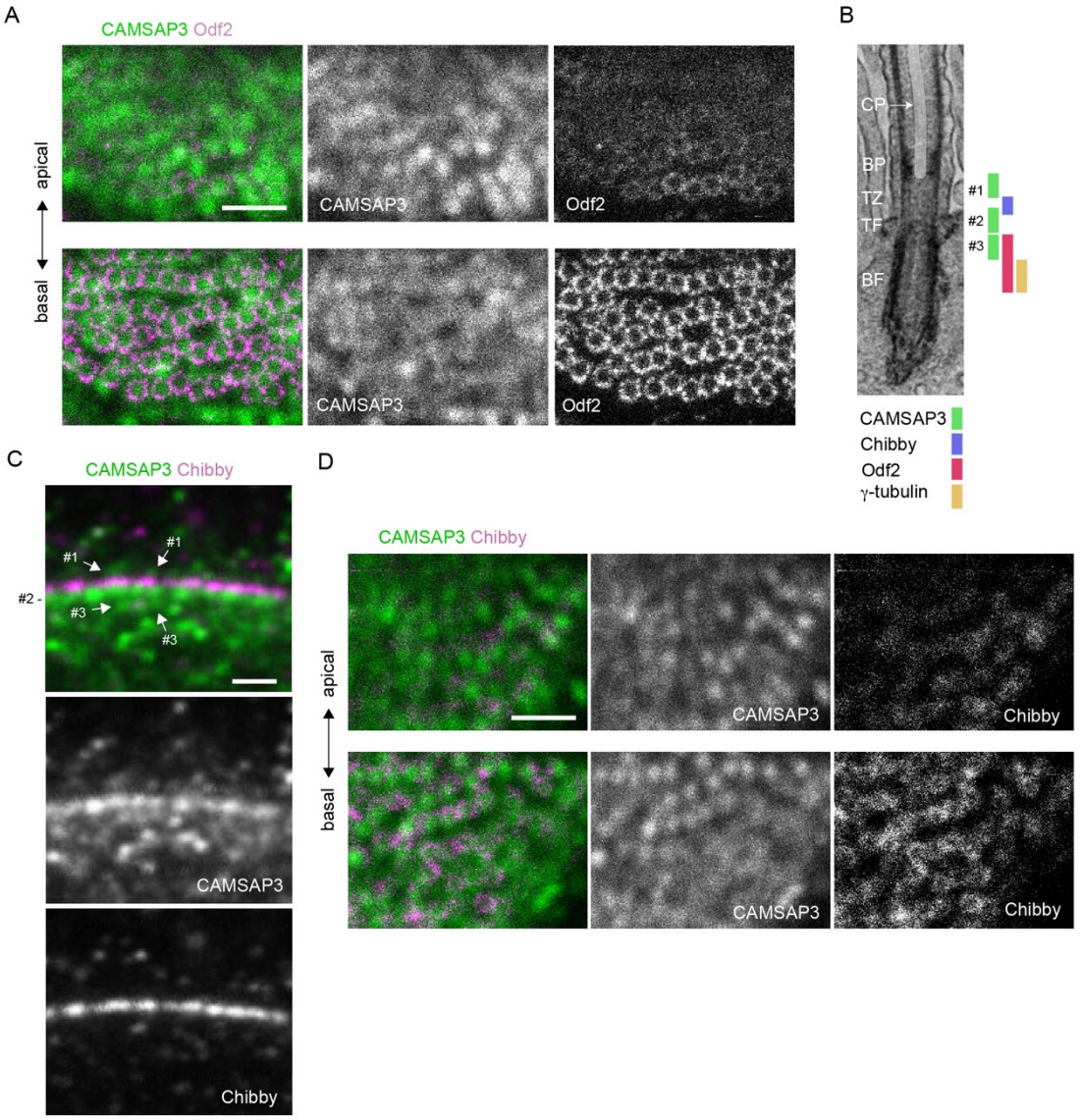

Figure 5. CAMASP3 localization in the transition zone.

A. Horizontal views of a wild-type multiciliated cell, co-immunostained for CAMSAP3 and Odf2, and recorded by confocal (for CAMSAP3) and STED (for Odf2) microscopy. The images at two horizontal levels, which are 0.4 μm apart, are shown. Oral side is at the bottom. The same samples were used in Movie 5. Trachea were collected from P180 mice and fixed with methanol in all the experiments shown in this figure.

B. Summary of the localization of the molecules studied, which is drawn next to an electron microscopical image of a single cilium. The CP is overlaid with a

semitransparent white color. The positions of Chibby and Odf2 were estimated using published data (Burke et al., 2014; Kunimoto et al., 2012). CP, the central pair of microtubules; BP, basal plate; TZ, transition zone; TF, transition fiber; BF, basal foot.
C. Vertical view of a wild-type multiciliated cell, co-immunostained for CAMSAP3 and Chibby, and recorded by confocal microscopy. Positions of the three rows of CAMSAP3 puncta are indicated.
D. Horizontal views of a wild-type multi-ciliated cell, co-immunostained for CAMSAP3 and Chibby, and recorded by confocal (for CAMSAP3) and STED (for Chibby) microscopy. The images at two horizontal levels, which are 0.4 μm apart, are shown. Oral side is at the bottom. The same samples were used in Movie 6.
Scale bars, 1 μm.

Figure 6

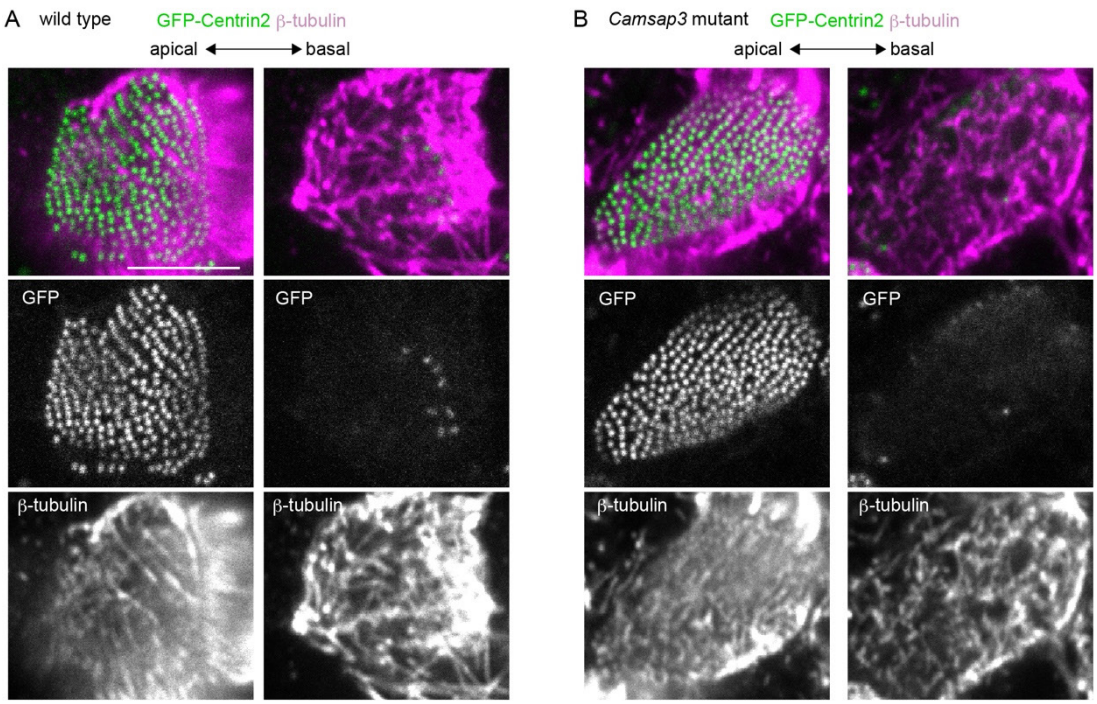

Figure 6. Microtubule distribution at the apical portions of a multiciliated cell.
β-tubulin was immunostained using trachea isolated from a wild-type (A) or *Camsap3*$^{dc/dc}$ (B) mouse expressing GFP-Centrin2. The images at two horizontal levels, which are 0.12 (in A) and 0.10 μm (in B) apart, are shown. Oral side is at the right. P180 mice were used. The same samples were used in Movies 7 and 8.
Scale bars, 5 μm.

Movie legends

Movie 1. Beating multicilia in a wild-type airway epithelial cell. The time-lapse images were acquired at 300 fps and displayed at 31 fps.

Movie 2. Beating multicilia in a *Camsap3*-mutated airway epithelial cell. The time-lapse images were acquired at 300 fps and displayed at 31 fps.

Movie 3. Beating multicilia in a wild-type airway epithelial cell, which is overlaid with a flow vector field calculated by PIV analysis. The white scale arrow and scale bar are 20 μm/s and 1 μm, respectively. Part of Movie 1 was used for this analysis.

Movie 4. Beating multicilia in a *Camsap3*-mutated airway epithelial cell, which is overlaid with a flow vector field calculated by PIV analysis. The white scale arrow and scale bar are 20 μm/s and 1 μm, respectively. Part of Movie 2 was used for this analysis.

Movie 5. Animation of sequential optical sections, each of which is 0.1 μm thick, of a wild-type multi-ciliated epithelial cell, co-immunostained for CAMSAP3 (green) and Odf2 (magenta). The animation view begins at the level where the #2 row of CAMSAP3 is detectable, then shifts toward a more basal view of the cell at a speed of 2 fps. See also Figure 4B.

Movie 6. Animation of sequential optical sections, each of which is 0.1 μm thick, of a wild-type multi-ciliated epithelial cell, co-immunostained for CAMSAP3 (green) and Chibby (magenta). The animation view begins at the level where the #1 row of CAMSAP3 is detectable, then shifts toward a more basal view of the cell at a speed of 2 fps. See also Figure 5B.

Movie 7. Animation of sequential optical sections, each of which is 0.2 μm thick, of a wild-type multi-ciliated epithelial cell, in which GFP-Centrin (green) and β-tubulin (magenta) are visualized by fluorescence signals. The animation view begins around the level where the array of GFP-Centrin is detectable, then shifts toward a more basal view of the cell at a speed of 2 fps. See also Figure 6A.

Movie 8. Animation of sequential optical sections, each of which is 0.2 μm thick, of a *Camsap3*-mutated multi-ciliated epithelial cell, in which GFP-Centrin (green) and β-

tubulin (magenta) are visualized by fluorescence signals. The animation view begins at the level where the array of GFP-Centrin is detectable, then shifts toward a more basal view of the cell at a speed of 2 fps. See also Figure 6B.

Audio legends

Audio 1. Respiratory sound of a P50 *Camsap3* mutant mouse.

Supplementary Table 1. Optical conditions to capture STED images.

	1st antibody	2nd antibody	Excitation	Laser power	Emission	STED	STED laser power		Fig. No.
1	Odf2	STAR635P	635nm	10%	645-750nm	775nm	100%	STAR635P→ Alexa488 (Between frames)	Fig. 5A
	CAMSAP3	Alexa488	488nm	10%	510-530nm	OFF	0%		Movie. 5
2	Chibby	STAR580	580nm	15%	590-620nm	775nm	30%	STAR580 → Alexa488 (Between frames)	Fig. 5D
	CAMSAP3	Alexa488	488nm	10%	510-530nm	OFF	0%		Movie. 6